10.2514/6.2015-1519

AIAA SciTech Forum
5-9 January 2015, Kissimmee, Florida
53rd AIAA Aerospace Sciences Meeting

Unsteadiness characteristics and pressure distribution of an oblique shock train

Robin L. Klomparens* , and James F. Driscoll† , Mirko Gamba‡

University of Michigan, Ann Arbor, MI 48109

Schlieren movies and pressure measurements were collected to analyze the quasi-steady state properties of an oblique shock train generated in a Mach 2.75 ducted flow and stabilized by a back-valve. Different values of back pressure (p_b) were considered to generate the shock train. Schlieren movies were processed with an edge detection algorithm to locate the shocks in the first interaction of the shock train. The shock train location was found to have a linear relationship with back pressure. More unsteady motion was found in the case with lower p_b. The maximum amplitude of the shock displacement was $0.9H$. In most cases, there was a dominant frequency of 145 Hz in both the shock position and speed power spectra. The highest back pressure case showed no dominant peak in the spectra. The average shock location was taken from Schlieren results and compared with pressure measurements. The shock location coincided with the start of the pressure rise and the local peak in the pressure standard deviation. Three-dimensional effects were evident from the comparison of side- and bottom-wall measurements. The side-walls had local maximum in the pressure profile likely due to the thin side-wall boundary layer. Bottom-wall pressure profiles were nearly linear. Finally, the shape of the time-averaged pressure distribution compared well with previous experimental and theoretical results.

Nomenclature

x	Coordinate in the stream-wise direction
y	Coordinate in the transverse direction
z	Coordinate in the vertical direction
u	Velocity component in the x-direction
M	Mach number
Re	Reynolds number
D	Diameter
p	Static pressure
θ	Momentum thickness
δ	Boundary layer thickness
H	Test section height = 2.75 in (69.85 mm)
W	Test section width = 2.25 in (57.20 mm)
α	Shock angle
Δ	Change in property referenced from the average
σ	Standard deviation

Subscript

a	Condition at the beginning of the test section
b	Condition at the end of the test section
0	Condition at the beginning of the pressure rise ($p > 1.05p_a$)
s	Property of the shock

*Graduate Research Assitant, Dept. of Aerospace Engineering.
†Arthur B. Modine Professor, Dept. of Aerospace Engineering, AIAA member.
‡Assistant Professor, Dept. of Aerospace Engineering, AIAA member.

I. Introduction

In high-speed air-breathing engine designs, the isolator separates the inlet from the combustor. An increased pressure from the combustion process causes the formation of multiple coupled shock waves, and thus multiple coupled shock boundary layer interactions. This system of shocks is known as a shock train. Depending on the entrance conditions, such as Mach number and pressure, the shock train can consist of normal or oblique shocks. A normal shock train generally has a leading bifurcated shock followed by several non-bifurcated shocks. In an oblique shock train, a right-running and left-running shock are generated from opposite walls of the duct. These shocks cross to form an "X" pattern. Multiple "X" structures form the shock train. After the shock train is a mixing region where no shocks are present but the pressure increases to some extent.[1] The entire region from the beginning of the shock train to the end of the mixing region is known as a pseudo-shock. If the pressure rise is too large, inlet unstart occurs, where the shock system is disgorged from the inlet. It is therefore important to understand the development of the shock train and the associated boundary layer separation in order to better understand the events leading up to unstart.

There have been numerous previous studies that have looked at the structure of shock trains in supersonic duct flows as a function of wind tunnel parameters. Matsuo et al.[1] have a comprehensive summary on some of these effects. Carroll and Dutton[2] found a tendency for a normal shock train to transition to oblique shocks with increasing Mach number. They also observed an increase in the number of shocks and the spacing between shocks with Mach number. As a result, the shock train becomes longer and exhibits more boundary layer separation.

Nill and Mattick[3] found similar trends for increasing the flow confinement, defined here as the ratio of boundary layer thickness to test section half height. As the length of the duct increases in front of the shock system, more momentum is lost to the boundary layer which makes the shock system longer, with more spacing between shocks. Oblique shock trains seem to be less sensitive to these changes than normal shock trains. The flow confinement can be altered by changing the overall pressure differential across the isolator. The shock train moves to a new position, with a different boundary layer thickness, to match the imposed pressure rise.[4]

Boundary layer effects are also strongly evident in pressure measurements. Pressure peaks from distinct shocks are typically not visible in the wall pressure distribution due to the dissipative character of the boundary layer.[5] In the experiment by Sullins and McLafferty[6] the pressure rise was the same for all four side-walls even though the boundary layers are significantly different. This suggests that significant communication between regions occurs through the boundary layer. However, this result is not always evident in other experiments and the character of the boundary layer likely plays a role in the exact formation of shock trains.

Oddly enough, many studies have shown that the shape of the side-wall pressure distribution is independent of the location of the shock train in the duct.[2,7] This seems to contrast the earlier discussion on the effects of flow confinement. The boundary layer thickness will alter the shock train structure, such as spacing between the shocks, but not the side-wall pressure distribution. Waltrup and Billig used experimental data with varied Mach number and cross sectional size to create a simple quadratic relationship to represent all the data.[7] They found the following relation:

$$\frac{x(M_a-1)Re_\theta^{1/4}}{(D\theta)^{1/2}} = 50\left(\frac{p}{p_a}-1\right)+170\left(\frac{p}{p_a}-1\right)^2 \tag{1}$$

While this relationship was determined based on results from a circular cross section wind tunnel, it still applies to rectangular cross-sections with surprisingly minimal difference.[8,9] The relation captures the dependence on flow Mach number, Reynolds number, free-stream pressure, boundary layer properties, and duct geometry. The system clearly has a complex reliance on many various parameters.

Computational fluid dynamics (CFD) has also been employed to determine the structure of shock trains. Earlier attempts by Carroll et al. used the explicit, time-dependent, second-order accurate MacCormack scheme to solve the mass-averaged Navier-Stokes equations.[10] The computations accurately predicted major features of the shock train in a Mach 1.6 flow, such as centerline Mach number and side-wall pressure, but failed to properly model the flow separation. Computations by Cox-Stouffer and Hagenmaier solved the three-dimensional Reynolds-averaged conservation equations for perfect gases with a cell-centered finite volume scheme.[11] The results showed that increasing the aspect ratio lead to a longer shock train with the shocks stabilizing further upstream. The trends agree with experimental results but the numbers were never directly compared.

Morgan et al.[12] used large-eddy simulations (LES) to model the normal shock train in a constant area duct experiment of Carroll and Dutton.[2] The LES results show good agreement in flow structure when the data was shifted in the stream-wise direction to match the beginning of the shock train in the experiment. The results changed drastically when the side-walls were fully resolved because the leading shock bifurcation caused side-wall separation and additional flow blockage. Although qualitative, the side-wall separation is a similar size and shape to the one measured in experimental studies. This emphasizes the importance of three-dimensional effects on shock train development leading up to unstart.

The above studies are clear evidence that the shock train flow structure is connected with the boundary layer properties. In a realistic low aspect ratio isolator, the multiple separation zones may interact with each other in complex three-dimensional ways. As the amount of separation increases, the core flow becomes more restricted and the state of the boundary layer will affect the unstart dynamics.[13] One of the major problems with predicting the shock train properties for a set of given boundary conditions is the inherent unsteadiness of the system. Matsuo et al. termed these fluctuations "self-excited oscillations."[1] The movement of the shock is coupled with pressure oscillations in the duct which may generate noise or fluctuating wall loads, both of which need to be minimized.

There are a limited number of studies that focus on shock train oscillations. It is clear that increasing the Mach number tends to increase the unsteadiness of the system.[2] However, there are conflicting answers to how the flow confinement changes the unsteadiness.[3,14] Miyazato et al. looked into the position of the shocks using pressure measurements and found that the first shock was strongly correlated with the following shocks, indicating that all of the shocks in the system have the same phase delay.[15] The cause of the unsteadiness must somehow have an equal impact on all the shocks in the system.

The mechanism behind these fluctuations remains unclear. Yamane et al. measured pressure at several points to determine the correlation coefficient and coherence.[16] The results pointed to an upstream propagating disturbance as the source of high frequency oscillations. Little to no damping was evident when the shock train was moved to a new location in the duct. A second, low frequency disturbance was well correlated with a downstream propagating disturbance. These low oscillations reduced when the shock train moved downstream.

Sugiyama et al. conjectured the cause of the oscillations to be within the shock train region.[17] Based on schlieren results, a kind of throat is formed between the first and second shocks due to the boundary layer thickness change. As the throat area decreases, the first shock moves upstream thereby reducing the incoming boundary layer thickness and amount of separation. Further evidence for this is seen using a shear stress-sensitive liquid crystal method.[14] The separation regions can be seen with this method but the results are purely qualitative. Still today, much about the unsteady aspect of shock trains is not understood.

A similar large scale, low frequency unsteadiness has been observed in many single shock-wave/boundary-layer (SBLI) experiments.[18–20] The source of the unsteadiness is still open to debate. It is likely that upstream turbulent structures interact with the separation region in addition to downstream instabilities, with the magnitude of each disturbance dependent on the strength of the SBLI.[21] However, for the shock train, the multiple separation regions can interact in complex ways.[22] A detailed look at the separation regions is required to further investigate the unsteady motion observed.

The goal of the current work is to examine the shock train unsteadiness characteristics and pressure profile. This is in preparation for looking at the specific boundary layer structure and three-dimensionality of this complex system. Ultimately, a better understanding of the overall shock train physics can be developed. This would be a bridge between the single SBLI work and previous studies on shock train structure. A better understanding of the flow structure in a realistic system with multiple, coupled interactions, could aid in the detection and prevention of unstart.

II. Experimental Setup

The current experiments were performed in a Mach 2.75 suction type wind tunnel at the University of Michigan.[23] The wind tunnel has a one-sided converging-diverging nozzle that provides the supersonic flow to the low aspect ratio test section which measures 57.2 x 69.83 mm. The constant area, rectangular cross-section mimics the geometry of a typical isolator. The unit Reynolds number for the experiment is 8.9×10^6/m. Borosilicate glass side-walls and bottom-wall plug provide optical access into the wind tunnel.

A shock train is produced by partially closing a VAT series 612 butterfly control valve separating the diffuser and vacuum chamber. The reduced area for airflow increases the back pressure p_b and a shock

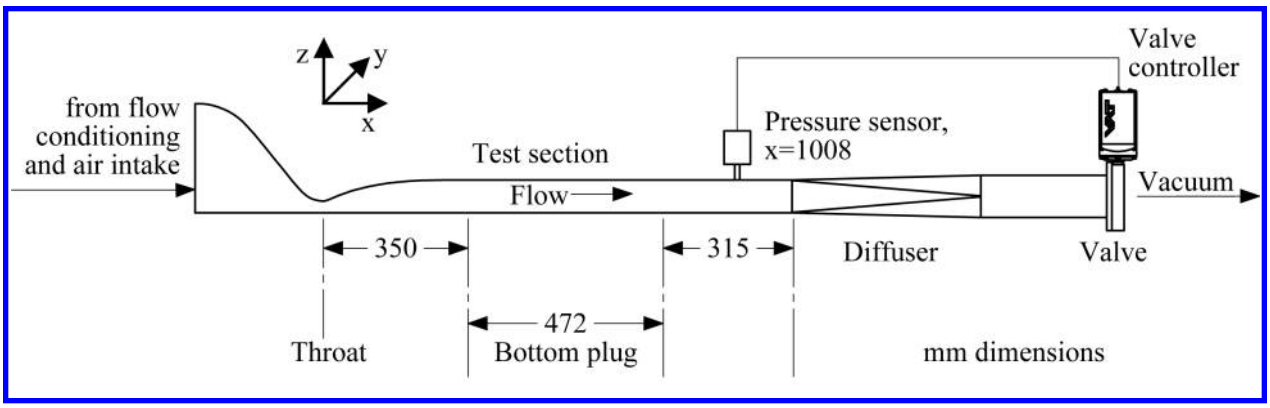

Figure 1. Schematic diagram of the wind tunnel.

structure must be formed in the test section to match the pressure differential. The pressure just upstream of the diffuser is measured with an MKS 626C capacitance manometer. The accuracy of the manometer is 0.25% of the reading and the response time is about 0.2 msec. The pressure reading is input to the valve and a control algorithm changes the angle of the valve plate in order to maintain the desired back pressure. The standard deviation in back pressure for a typical run is 0.1 kPa. Some of this deviation from the mean value is due to turbulence in the downstream flow. A schematic of the wind tunnel is shown in figure 1.

A right-handed coordinate system is used for this work. The x-direction is oriented streamwise and the z-direction is normal to the bottom-wall. The origin is located on in the lower right corner of the duct cross-section as one looks downstream.

Schlieren imaging and bottom- and side-wall static pressure measurements are presented in this paper. Five cases are summarized in table 1. Case 0 is when the valve is completely open and no shock train exists. This is the baseline (undisturbed) flow and it is the basis for comparison with the primary cases which have a raised back pressure at the MKS sensor location. The back pressure values reported here are normalized with the value upstream of the shock train, p_a. p_a is found given the total pressure of the room (measured before each run) and the known pressure ratio across the nozzle of the wind tunnel. Case 1 has the lowest back pressure and is the farthest downstream. Case 4 has the highest back pressure and the shock train sits upstream, closest to the throat. Cases 2 and 3 have intermediate back pressures. Cases 2 and 4 are frequently used as examples in the results section. However, all of the cases were considered when determining trends.

The incoming boundary layer thickness for the top and bottom-walls are also reported in table 1 for all the cases containing a shock train. The boundary layer thickness, δ, was found from the schlieren images by locating the point of maximum intensity change. These numbers compare well to earlier PIV measurements of the boundary layer available at selected locations.[24] Finally, the confinement ratio, C, which is defined as the ratio between boundary layer thickness and channel half-height, was calculated using the average boundary layer thickness.

The schlieren system is used to identify the shock location and visualize qualitative changes in the boundary layer. A folded z-type setup with a horizontal knife-edge captures vertical gradients in the flow. The light source was fabricated in-house and uses a Luminus SBR-70 LED for continuous illumination. Images were recorded with a Phantom 711 camera at a rate of 8,000 Hz with an exposure time of 2 μs. Each image has a resolution of 576 $\times$ 288 pixels. The field of view is roughly 135 mm in the stream-wise direction

Table 1. Summary of experimental conditions.

Case	0	1	2	3	4
p_b/p_a	1.5	5.3	5.7	6.2	6.6
top-wall δ_a	-	8.5	7.9	7.1	6.2
bottom-wall δ_a	-	10.0	9.1	7.6	6.5
C	-	0.26	0.24	0.21	0.18

by the full tunnel height, H. Multiple schlieren images had to be stitched together to visualize the entire shock train.

Static pressure measurements are taken in order to gain insight on the average shock train structure. The glass side-walls and bottom-wall plug can be replaced with aluminum pieces containing pressure taps. Measurements are made with a Scanivalve DSA3217 digital sensor array at a rate of 20 Hz. The pressure taps are located along the centerline, $y=W/2$ and $z=H/2$, for the bottom- and side-wall, respectively. Wall pressure taps were spaced 12.7 mm apart for high spatial-resolution results.

III. Results

A. Schlieren

The schlieren movies provide an effective way of determining the boundary layer structure and can be a qualitative estimate on the amount of boundary layer separation. For example, figure 2a and b are stitched images of multiple instantaneous schlieren snapshots for cases 2 and 4, respectively. The most upstream pair of oblique shocks cross to form the leading "X" structure. The second "X" is confined in a much smaller, turbulent core flow. Keep in mind that the images are from different runs because of the limited field of view of the schlieren system. The downstream "X" structures are in a more turbulent flow and are not always completely visible. It is also evident that the flow is not symmetric. The bottom-wall has a much thicker boundary layer than the top-wall due to the asymmetry of the wind tunnel nozzle. This impacts the shape of the shock train. For example, the intersection of the shocks in a given "X" is closer to the top-wall. As expected, the lower back pressure case has a thicker incoming boundary layer compared to the higher back pressure case. In case 2, the flow is more confined to begin with but also shows more boundary layer growth.

Even though the back pressure is held constant, the shock train exhibits some inherent unsteadiness. The schlieren movies were recorded at a fast enough frequency to analyze the motion of the shocks. Raw image files were processed using MATLAB to automatically detect the shock location. First, a Sobel filter was used to find edges in the image. Most of the edges from free-stream turbulence were removed with a median filter. The result can be seen in figure 3a. Lines were then extracted from the image with a Hough transform and the line associated with the shock was picked based on the angle and location compared to the previous image. Figure 3b is an example of the leading X shock locations traced over the original image. The solid black line is the left-running (LR) wave and the solid white line is the right-running (RR) wave,

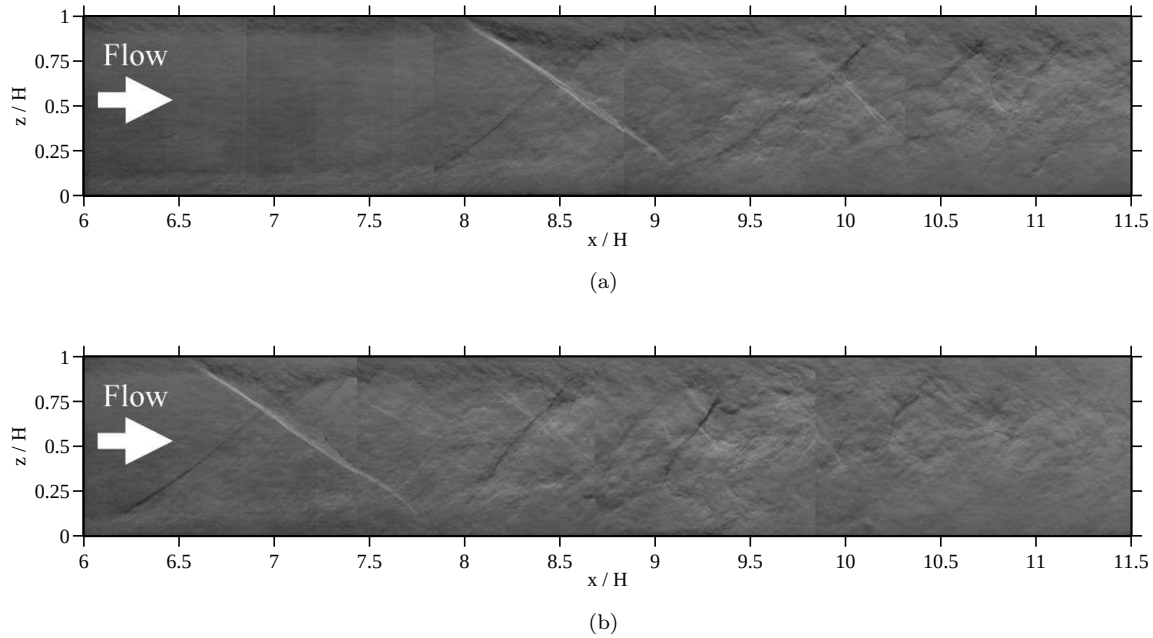

Figure 2. Instantaneous schlieren images: (a) case 2; and (b) case 4.

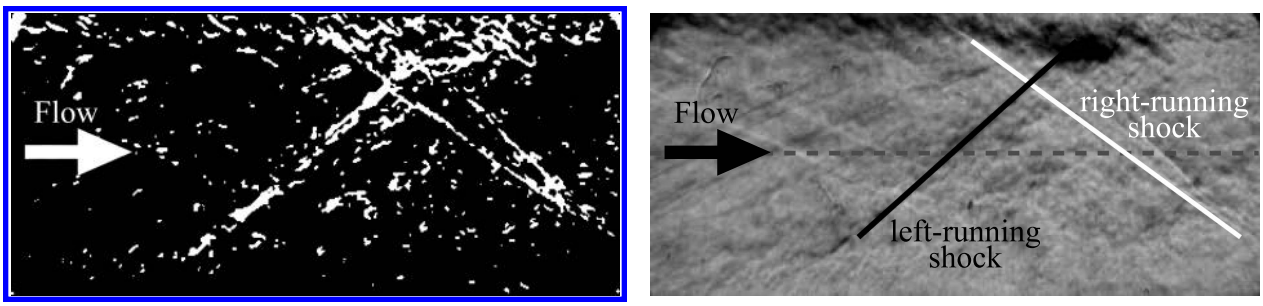

(a) (b)

Figure 3. Example of the MATLAB edge detection algorithm developed in this work: (a) Image after the Sobel operator; (b) original image with detected edges (LR and RR oblique shocks).

the two most upstream shocks in the system. Centerline is marked by the grey dashed line.

The centerline location (z=$H/2$) of each shock, x_s, and the angle of the shock with respect to the x-axis, α, were tracked with time. The leading RR shock could be accurately detected in over 99.9% of the images. The leading LR shock was harder to locate because the magnitude of the intensity change was consistently lower than that of the RR shock. In the worst case, the LR shock was detected in 95.6% of the images. If the shock could not be detected, the image was skipped and the x-location was set equal to that of the previous image. In most of the skipped images the shock was not visible by eye. Other sources of error for this edge detection method stem from the shape of the shock itself. Some shocks are slightly curved towards the wall and others have a discontinuity along the line of constant intensity. These errors were minimized by restricting the edge detection algorithm to the core flow, away from the boundary layer.

The shock angles appear constant based on multiple measurements of the different back pressure cases. The average angle of the RR shock is $-55.5°$. The standard deviation during a typical run is $1.0°$, meaning the shock angle does not change much with time. Some of this deviation is due to measurement error in the edge detection algorithm. The run-to-run standard deviation is $1.6°$ indicating fairly consistent measurements across all back pressure cases. The average angle of the LR shock is $52.6°$. This shock was harder to detect and consequently has a higher per run standard deviation of $2.2°$. The run-to-run standard deviation is $2.9°$. Based on these results, we can conclude that the shock angle remains fairly constant with time and is independent of the back pressure.

Next, the normalized shock position, x_s/H, was analyzed. A Gaussian filter with a size of 11 points and a standard deviation of 0.75 was used to smooth the position data. The average shock position for each individual run is plotted versus the pressure ratio, p_b/p_a in figure 4. The error bars for each point represent ± 1 standard deviation in the measurements for that particular run. A linear fit with an R^2 value of 0.97 is also shown. There is a clear linear relationship between the pressure ratio and the position of the shock train.

A portion of the time trace showing the locations for both the leading LR and RR oblique shocks in a shock train can be seen in figure 5a. Only cases 2 and 4 are plotted as an example. The leading LR and RR shocks for a particular case of back pressure are highly correlated and there is no time lag between the two. The average correlation coefficient is 0.91. Statistics on the shock position fluctuations can be found directly from the time trace and are summarized in table 2.

Cases 1-3 suggest that a higher back pressure leads to smaller fluctuations in the shock position. The most downstream case has fluctuations with the highest amplitude and standard deviation. However, the most upstream case goes against this trend. It could be that case 4 is so close to unstarting the tunnel that the shock position fluctuations have suddenly increased. More data at this upstream location needs to be taken in order to resolve this conflict. In each case the LR and RR shocks have similar fluctuation position statistics. The difference between the values may be due to measurement error.

The instantaneous deviation of the shock position from its time-average position can be as large as 0.9 tunnel heights. This compares well with the limited number other unsteadiness studies on oblique shock trains. Sugiyama et al.[17] and Ikui et al.[25] had experiments with Mach numbers of 4 and 2.79, respectively, and found the maximum oscillation amplitude to be 1 duct height (or diameter).

Information on the shock train position can also be visualized from the probability density function (PDF)

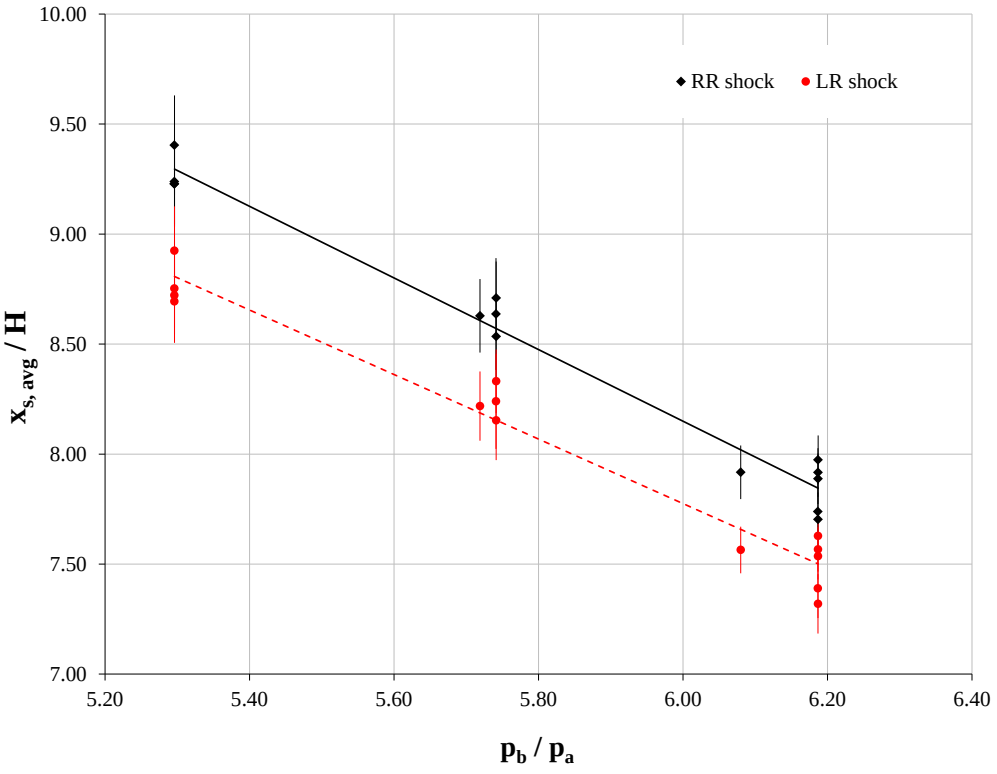

Figure 4. Average shock location versus back pressure ratio.

of the shock location, seen in figure 5b. One interesting aspect is that the upstream tail of the distributions are slightly longer than the downstream side. The maximum deviation from the mean position typically happens when the "X" quickly travels upstream. Finally, figure 5c is the power spectral density (PSD) of the shock position. Case 2 has a clear peak at 145 Hz whereas case 4 has no clear peak in the power spectra. While not shown, cases 1 and 3 also have power spectra similar to case 2 with dominant peaks between 133 and 160 Hz, suggesting a dominant frequency.

The shock speed was found from the time-history measurement of the shock position as the difference between consecutive positions. Figure 6a shows the time trace of the shock speed normalized by the freestream value (u_a = 593 m/s). Once again, only cases 2 and 4 are shown for clarity. Some statistics on the shock speed are shown in table 2. The time trace shows that the LR and RR shock speeds for a given back pressure are not as highly correlated as the shock positions. The average correlation coefficient is 0.36 at a time lag of 0 seconds. Be believe that part of the degradation of the correlation coefficient is due to noise. Overall, the statistics are fairly consistent and seem to be independent of back pressure. The LR shock speeds have higher maximum values than the RR shock. The LR shock has a maximum shock speed of 0.24 u_a whereas the RR shock reaches speeds of only 0.19 u_a.

The probability density function in figure 6b demonstrates the similarity in shock speed statistical values. All distributions have the same peak value and standard deviation. Finally, the power spectral density of speed, shown in figure 6c, has the same peak frequencies as the shock position power spectra. The peaks are much more noticeable in the speed power spectra. Case 2 has a local peak at 145 Hz and case 4 has no clear peak. Cases 1 and 3, while not shown, also have a dominant frequency in the 133-160 Hz range. The current experimental result falls within the range of dominant frequencies found by others. Ikui et al.[25] noted a major peak in the power spectra at 40 Hz and smaller peaks between 40-200 Hz for a Mach 2.75 flow. Sugiyama et al.[14] found peaks below 100 Hz and at about 190 Hz for a Mach 4 flow with a confinement ratio of 0.39.

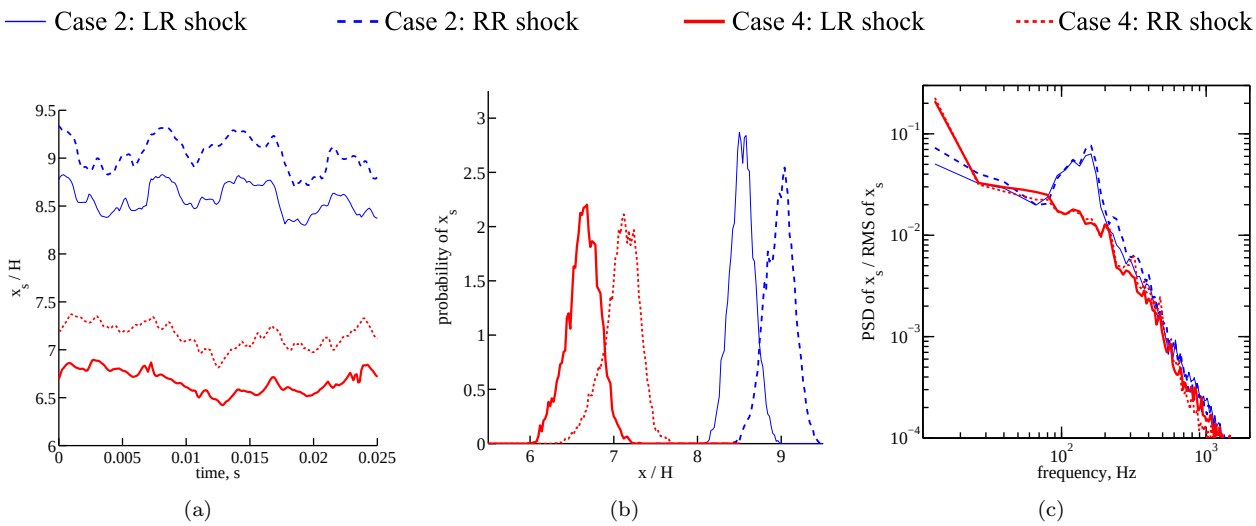

(a) (b) (c)

Figure 5. Analysis of the leading LR and RR shock location: (a) time trace; (b) probability density function; and (c) power spectral density.

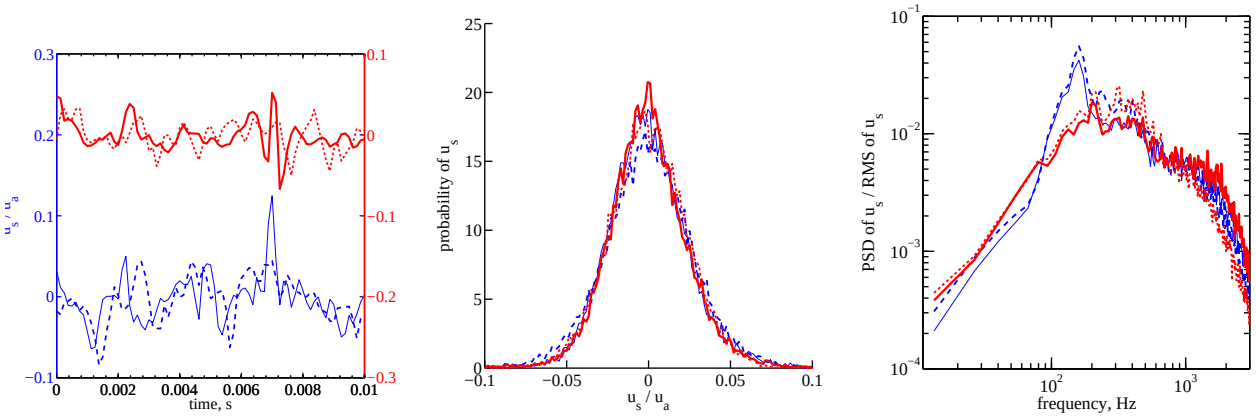

(a) Time trace (b) Probability density function (c) Power spectral density

Figure 6. Analysis of the leading LR and RR shock speed: (a) time trace; (b) probability density function; and (c) power spectral density.

Table 2. x-location and shock speed statistics.

Case	Shock	Average x_s	Maximum ($\lvert\Delta x/H\rvert$)	σ ($\Delta x/H$)	Maximum ($\lvert u_s/u_a\rvert$)	σ (u_s/u_a)
1	RR	9.27	0.90	0.20	0.18	0.02
1	LR	8.77	0.82	0.19	0.23	0.02
2	RR	8.71	0.78	0.18	0.15	0.02
2	LR	8.30	0.71	0.16	0.24	0.02
3	RR	7.81	0.53	0.12	0.14	0.02
3	LR	7.45	0.56	0.13	0.20	0.02
4	RR	7.11	0.80	0.21	0.19	0.02
4	LR	6.64	0.88	0.20	0.23	0.02

B. Pressure

Unlike the schlieren measurements, the pressure data cannot be used to study the unsteadiness because the measurements were only taken at 20 Hz. However, the averaged results can be used to compare with other experiments and shock train models. Figure 7a shows the side- and bottom-wall pressure measurements versus the nondimensional tunnel x-location for cases 2 and 4. For comparison, the pressure rise for a normal shock at $M = 2.75$ is given. From these profiles we conjecture that the bottom-wall has a thicker, more separated boundary layer because of the smoother pressure distribution. The side-wall pressure peaks for the downstream case are less distinct and using the same reasoning, this case likely has a thicker boundary layer.

The location where the pressure rises above $1.05p_a$ is called x_0. This value was compared to the LR shock foot (z=0) and centerline (z=$H/2$) locations. These numbers were taken directly from the schlieren analysis and the shock foot was extrapolated using the centerline location and the angle of the shock. The shock locations correspond to the pressure measurements they are physically closest to. In both cases 2 and 4 the centerline shock location trails x_0 of the side-wall pressure rise by $0.46H$. Similarly, the shock foot location is $0.57H$ downstream of the beginning of the bottom-wall pressure rise. The pressure begins to rise upstream of the shock location because information is transferred upstream through the (subsonic portion of the) boundary layer.

The standard deviation of the pressure measurements, σ, is shown in figure 7b. Case 2 (downstream) has a smaller standard deviation than case 4 which agrees with the results found from the schlieren analysis. Bottom-wall measurements show much less deviation from the mean value than side-wall measurements. Once again, this is likely because the boundary layer is thicker on the bottom-wall, and thus stifles the effects of the shocks. Finally, the shock locations from the schlieren analysis were compared with the position of the first peak of the pressure standard deviation profiles. In general, the shock foot extracted from the schlieren images is downstream of the point of maximum σ. In particular, the shock foot is downstream of the bottom-wall maximum σ by $0.40H$ and $0.20H$ for case 2 and 4, respectively. Furthermore, the centerline shock location is $0.27H$ and $0.34H$ downstream of the peak σ on the side-wall for each respective case. In both instances, the shock locations are closer to the peak in pressure standard deviation than to the beginning of the pressure rise itself (i.e., to the start of the upstream region of influence). This is evidence

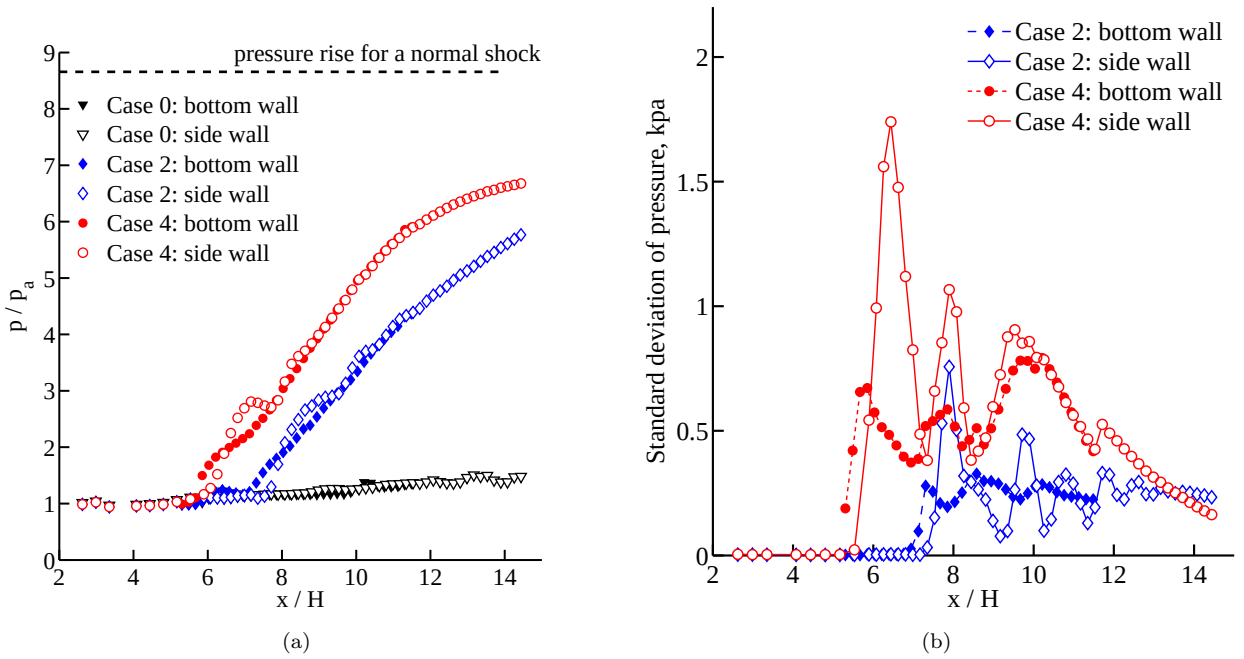

Figure 7. (a) Comparison of streamwise wall static pressure distribution for cases 0, 2, and 4 (on side- and bottom-walls); (b) distribution of the standard deviation of wall static pressure measurements as a function of streamwise distance.

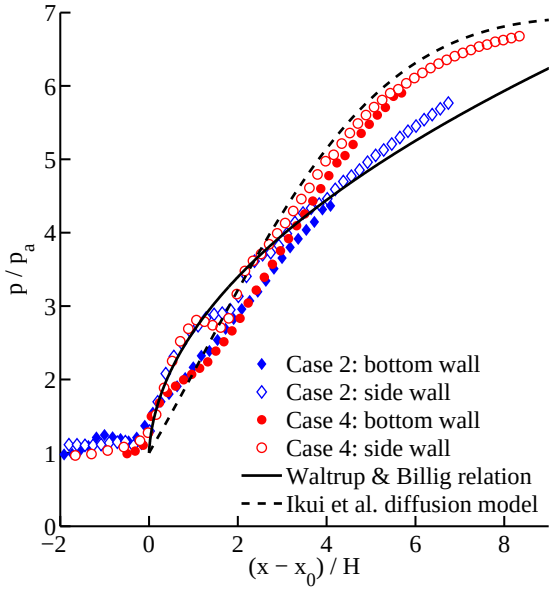

Figure 8. Wall static pressure distribution with shifted x-axis.

that the movement of the first shock is the source of the pressure fluctuations. The remaining peaks in standard deviation downstream of the first one could be due to fluctuations of the downstream X-cells in the shock train system.

As mentioned before, many studies have shown that the average side-wall pressure distribution is independent of the back pressure. Even as the shock train moves upstream or downstream, the pressure profile remains the same, just shifted to a new starting location. This result is demonstrated for the current experiment in figure 8 where the profiles of figure 7 have been shifted by x_0. The side- and bottom-wall profiles for different cases of back pressure have collapsed to similar curves for $(x - x_0)/H < 3$. However, at the more downstream locations (i.e., $(x - x_0)/H > 4$), the profiles for the two cases start to diverge. Interestingly, the region of $0 < (x - x_0)/H < 4$ can be recognized from the schlieren images to be the shock train region; therefore, the mixing region is when $(x - x_0)/H > 4$. Thus, it appears that the scaled pressure profiles collapse in the shock train region while they diverge in the mixing region. However, more work is required to clarify if this is a general result or simply a fortuitous coincidence for this specific set of experiments. At this time pressure profiles were taken only for case 0, 2, and 4.

Present data also agrees well with various shock train models. Ikui et al.[26] made improvements to Crocco's shockless model[27] for the pseudo-shock and developed a theoretical model for the pressure rise along the shock train. Figure 8 is a comparison between the current data set, Ikui's theoretical model, and the empirical relationship shown in Eq. (1). The hydraulic diameter was used for both calculations since the current experiment has a square test section. The side-wall pressure profiles agree well with Waltrup and Billig's relationship for $(x - x_0)/H < 2$ whereas the bottom-wall measurements follow the diffusion model at this stage. For $(x - x_0)/H > 2$ the upstream case has a slightly smaller magnitude but has the same curvature as the empirical formula. The downstream case is closer to the diffusion model.

IV. Conclusions

The quasi-steady state properties of a shock train were studied at four different back pressures. Schlieren movies proved to be a successful way to study the shock train's unsteady motion. Shock locations extracted from the schlieren images were then compared to side- and bottom-wall average pressure profiles. The results are summarized below.

1. There exists a linear relationship between back pressure and the average location of the shock train. Increasing the back pressure will move the shock train upstream to where the incoming boundary layer thickness (or equivalently the confinement ratio) is smaller.

2. The position of the right-running and left-running shocks that cross to form the upstream "X" were highly correlated with a correlation coefficient of at least 0.9 and a zero time lag. The shock speed was less correlated than the position with a correlation coefficient around 0.36. This could partially be due to noise.

3. There were shock position fluctuations of up to $0.9H$. Increasing the back pressure tends to decrease the severity of the fluctuations. However, this was not evident in the most upstream case, where tunnel unstart is imminent.

4. The distribution of shock speed seems to be independent of the back pressure. There was a maximum speed of $0.24u_a$.

5. Both the position and speed power spectra have a local peak near 145 Hz for 3 of the 4 cases considered here. The most upstream case has no dominant frequency.

6. The side-wall pressure distribution has a local peak corresponding to the location of the first "X". The bottom-wall pressure distribution is much smoother, likely because of the thicker boundary layer. For the same reason, the bottom-wall pressure fluctuations were smaller.

7. The shock foot position corresponds to the start of the pressure rise and the maximum standard deviation of the bottom-wall pressure. The centerline shock location more closely matches the start of the side-wall pressure rise and the peak in side-wall pressure standard deviation.

8. Finally, the pressure profiles from two cases had very similar shapes when compared on a relative axis. The experimental data reasonably follows the pressure profiles predicted by the empirical correlation of Waltrup and Billig and the diffusion model of Ikui et al.

Since each shock is coupled to the boundary layer growth and separation, the pressure rise is likely connected to the boundary layer in some way. A missing component in the literature is a quantitative investigation of the boundary layer, which could potentially tie into the self-similar pressure profile. This motivates future work.

Work conducted so far was aimed at getting a first-look at the general shock train properties for different back pressures. More work needs to be done to quantify the boundary layer properties of the shock train. In future work, PIV will be used to study the boundary layer in detail and attempt to clarify some of the 3D structures that were foreshadowed in the current paper. Our ongoing work will also continue to focus on the unsteady aspects of shock trains.

V. Acknowledgments

RLK acknowledges the financial support of the National Science Foundation Graduate Research Fellowship Program under Grant No. DGE 1256260. The author also appreciates the help of Rohan Morajkar in collecting some of the data presented here.

References

[1]Matsuo, K., Miyazato, Y., and Kim, H., "Shock train and pseudo-shock phenomena in internal gas flows," *Progress in Aerospace Sciences*, Vol. 35, No. 1, 1999, pp. 33–100.

[2]Carroll, B. and Dutton, J., "Characteristics of multiple shock wave/turbulent boundary layer interactions in rectangular ducts," *Journal of Propulsion and Power*, Vol. 6, No. 2, 1990, pp. 186–193.

[3]Nill, L. and Mattick, A., "An experimental study of shock structure in a normal shock train," *AIAA Paper No. 96-0799*, 1996.

[4]Lin, K., Tam, C., Jackson, K., Eklund, D., and Jackson, T., "Characterization of shock train structures inside constant-area isolators of model scramjet combustors," *AIAA Paper No. 2006-0816*, 2006.

[5]Om, D. and Childs, M., "Multiple transonic shock-wave/turbulent boundary-layer interaction in a circular duct," *AIAA journal*, Vol. 23, No. 10, 1985, pp. 1506–1511.

[6]Sullins, G. and McLafferty, G., "Experimental results of shock trains in rectangular ducts," *AIAA paper No. 92-5103*, 1992.

[7]Waltrup, P. and Billig, F., "Structure of shock waves in cylindrical ducts," *AIAA journal*, Vol. 11, No. 10, 1973, pp. 1404–1408.

[8]Bement, D., Stevens, J., and Thompson, M., "Measured operating characteristics of a rectangular combustor/inlet isolator," *AIAA paper No. 90-2221*, 1990.

[9]Lin, P., Rao, G., and O'Connor, G., "Numerical analysis of normal shock train in a constant area isolator," *AIAA paper No. 91-2162*, 1991.

[10]Carroll, B., Lopez-Fernandez, P., and Dutton, J., "Computations and experiments for a multiple normal shock/boundary-layer interaction," *Journal of Propulsion and Power*, Vol. 9, No. 3, 1993, pp. 405–411.

[11]Cox-Stouffer, S. and Hagenmaier, M., "The effect of aspect ratio on isolator performance," *AIAA paper No. 2001-0519*, 2001.

[12]Morgan, B., Duraisamy, K., and Lele, S. K., "Large-eddy simulations of a normal shock train in a constant-area isolator," *AIAA Journal*, Vol. 52, No. 3, March 2014, pp. 539–558.

[13]Do, H., Im, S., Mungal, M.G., Cappelli, M., "The influence of boundary layers on supersonic inlet unstart," *AIAA paper No. 2011-2349*, 2011.

[14]Sugiyama, H., Tsujiguchi, Y., and Honma, T., "Structure and oscillation phenomena of pseudo-shock waves in a straight square duct at mach 2 and 4," *AIAA paper No. 2008-2646*, April 2008.

[15]Miyazato, Y., Kashitani, M., and Matsuo, K., "Flow oscillation induced by normal shock wave/turbulent boundary-layer interaction in a supersonic diffuser," *Flow visualization VII*, 1995, pp. 853 – 8.

[16]Yamane, R., Takahashi, M., and Saito, H., "Vibration of pseudo-shock in a straight duct," *Bulletin of JSME*, Vol. 27, No. 229, 1984, pp. 1393–1398.

[17]Sugiyama, H., Takeda, H., and Zhang, J., "Locations and oscillation phenomena of pseudo-shock waves in a straight rectangular duct," *The Japan Society of Mechanical Engineers International Journal*, Vol. 31, No. 1, 1988, pp. 9–15.

[18]Humble, R., Scarano, F., and Van Oudheusden, B. W., "Unsteady flow organization of a shock wave/turbulent boundary layer interaction," *IUTAM Symposium on Unsteady Separated Flows and their Control*, Vol. 14, 2009, pp. 319–330.

[19]Larcheveque, L., Dupont, P., de Martel, E., Garnier, E., and Debieve, J. F., "Experimental and numerical study of unsteadiness in boundary layer / shock wave interaction," *Turbulence and Interactions*, Vol. 110, 2010, pp. 263–269.

[20]Ganapathisubramani, B., Clemens, N. T., and Dolling, D. S., "Low-frequency dynamics of shock-induced separation in a compression ramp interaction," *Journal of Fluid Mechanics*, Vol. 636, Sept. 2009, pp. 397.

[21]Clemens, N. T. and Narayanaswamy, V., "Low-frequency unsteadiness of shock wave/turbulent boundary layer interactions," *Annual Review of Fluid Mechanics*, Vol. 46, No. 1, Jan. 2014, pp. 469–492.

[22]Benek, J., Suchyta, C. I., and Babinsky, H., "The effect of wind tunnel size on incident shock boundary layer interaction experiments," *AIAA paper No. 2013-0862*, 2013.

[23]Lapsa, A. P., *Experimental study of passive ramps for control of shock boundary layer interactions*, Ph.D. thesis, 2009.

[24]Lapsa, A. P. and Dahm, W. J. a., "Stereo particle image velocimetry of nonequilibrium turbulence relaxation in a supersonic boundary layer," *Experiments in Fluids*, Vol. 50, No. 1, June 2010, pp. 89–108.

[25]Ikui, T., Matsuo, K., Nagai, M., Honjo, M., "Oscillation phenomena of pseudo-shock waves," *Bulletin of JSME International Journal*, Vol. 17, No. 112, 1974, pp. 1278–1285.

[26]Ikui, T., Matsuo, K., and Nagai, M., "The mechanism of pseudo-shock waves," *Bulletin of JSME*, Vol. 17, No. 108, 1974, pp. 731–739.

[27]Crocco, L., "One-dimensional treatment of steady gas dynamics," *Fundamentals of Gas Dynamics, High Speed Aerodynamics and Jet Propulsion*, Vol. 3, 1958, pp. 100–130.